Simple Geodesic Regression for Image Time-Series

Yi Hong[1], Yundi Shi[1], Martin Styner[1], Mar Sanchez[2], and Marc Niethammer[1]

[1] University of North Carolina (UNC), Chapel Hill NC 27599-3175, USA
yundiuu@gmail.com, {yihong,styner,mn}@cs.unc.edu
[2] Emory University, Atlanta GA 30322, USA
mmsanch@emory.edu

Abstract. Geodesic regression generalizes linear regression to general Riemannian manifolds. Applied to images, it allows for a compact approximation of an image time-series through an initial image and an initial momentum. Geodesic regression requires the definition of a squared residual (squared distance) between the regression geodesic and the measurement images. In principle, this squared distance should also be defined through a geodesic connecting an image on the regression geodesic to its respective measurement. However, in practice only standard registration distances (such as sum of squared distances) are used, to reduce computation time. This paper describes a simplified geodesic regression method which approximates the registration-based distances with respect to a fixed initial image. This results in dramatically simplified computations. In particular, the method becomes straightforward to implement using readily available large displacement diffeomorphic metric mapping (LDDMM) shooting algorithms and decouples the problem into pairwise image registrations allowing parallel computations. We evaluate the approach using 2D synthetic images and real 3D brain images.

Keywords: Geodesic regression, time-series, image registration.

1 Introduction

The increasing availability of longitudinal image time-series to study aging processes, brain development, or disease progression requires image analysis methods, and in particular image registration methods, customized for longitudinal data. A standard approach is to directly extend methods devised for pair-wise image registration to image time-series. In the case of LDDMM registration [1] a spatio-temporal velocity field is estimated over the full time-duration of the available measurements, with image similarity terms at the measurement time-points. This results in a piece-wise geodesic interpolation path [2,3] with jumps of the velocity field caused by the measurements.

To avoid these jumps, two directions have been pursued: (i) spline(-like) interpolations or general temporal smoothness terms (primarily for shapes) [4,5] or methods based on kernel regression [6] and (ii) approximations of time-series

B.M. Dawant et al. (Eds.): WBIR 2012, LNCS 7359, pp. 11–20, 2012.

through geodesic regression [7, 8]. While the former models are more flexible, geodesic regression directly yields a simple generative model which compactly parameterizes a full spatio-temporal trajectory using only an initial image and an initial momentum.

Geodesic regression seeks to minimize the sum of squared distances of the measurements to the regression geodesic. Closed-form solutions are generally not available. However, for some spaces analytical expressions for the "forces" exerted by the measurements on the regression geodesic (the equivalent to the model residuals for linear regression) can be computed [8]. Unfortunately, this is not the case when working with diffeomorphisms for image-valued geodesic regression [7]. Here, the squared distances can either be defined by registrations themselves, which is computationally expensive, or by using standard similarity measures for image registration (such as sum of squared intensity differences) assuming that all measurements are close to the regression geodesic.

This paper proposes an approximation to image-valued geodesic regression [7] *with registration-based distances* using a distance approximation for image-to-image registration proposed in [9]. This approximation allows for the computation of the regression geodesic (for a fixed initial image) by a weighted average of the initial momenta obtained by registering the initial image with the measurement images pairwise. Hence, standard shooting-based LDDMM implementation methods can be used for the computation of the regression geodesic and its computation decouples into pairwise registrations (see Fig. 1 for an illustration) which can be solved in parallel.

We motivate the weighting of the initial momenta for the image-valued case by illustrating the concept for linear regression in Sec. 2. Sec. 3 describes the image-valued case. To demonstrate the effectiveness of our scheme, we apply it to both synthetic and real image time-series in Sec. 4. We conclude and discuss future work in Sec. 5.

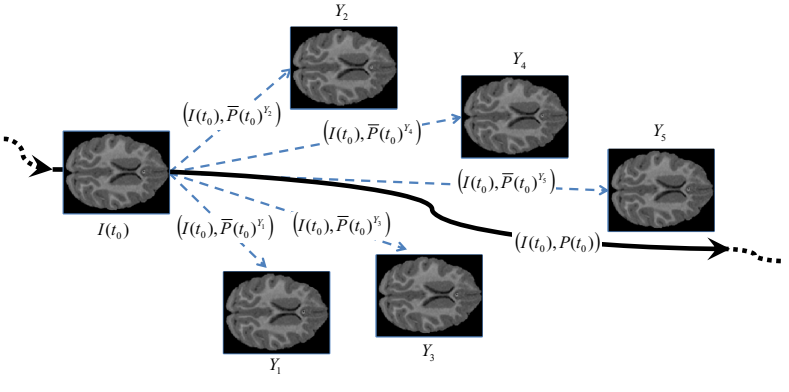

Fig. 1. Simple geodesic regression: the regression geodesic (bold) is determined by pairwise registrations between the base image, $I(t_0)$, and the measurement images, Y_i

2 Linear Regression (w/ fixed base-point) Reformulated

Given a set of N measurements $\{y_i\}$ at time instants $\{t_i\}$ we want to find the slope, a, and the y-intercept, b, of the best fitting line $y = at + b$ in a least squares sense. We assume that one point on this line is known[1]. Without loss of generality, we assume this point to be at the origin. Hence, we want to minimize

$$E(a) = \frac{1}{2}\sum_{i=1}^{N}(at_i - y_i)^2 \;\Rightarrow\; a = \frac{\sum_i y_i t_i}{\sum_i t_i^2}. \tag{1}$$

Assume that instead of fitting one line to all the measurements, we fit lines from the origin to all the measurement points individually. This amounts to independently minimizing

$$E_i(a_i) = \frac{1}{2}(a_i t_i - y_i)^2 \;\Rightarrow\; a_i = \frac{y_i}{t_i}. \tag{2}$$

Since $y_i = a_i t_i$, we obtain upon substitution in (1)

$$a = \frac{\sum_i t_i^2 a_i}{\sum_i t_i^2} = \sum_i w_i a_i, \quad \text{with} \quad w_i = \frac{t_i^2}{\sum_i t_i^2}, \;\; \sum_i w_i = 1. \tag{3}$$

Hence, the slope of the regression line can be computed as a weighted average of the slopes of the individual lines. What remains to be shown is that a similar averaging procedure can be used for the image-valued case.

3 Simple Geodesic Regression

Geodesic regression for image time-series generalizes linear regression to the space of images [7]. It uses a shooting formulation to LDDMM registration [11] and is based on the minimization of

$$E(I(t_0), p(t_0)) = \frac{1}{2}\langle p(t_0)\nabla I(t_0), K(p(t_0)\nabla I(t_0))\rangle + \sum_i w_i d^2(I(t_i), Y_i), \tag{4}$$

$$\text{s.t.} \qquad I_t + \nabla I^T v = 0, \;\; p_t + div(pv) = 0, \;\; v + K(p\nabla I) = 0, \tag{5}$$

where $I(t_0)$ and $p(t_0)$ are the unknown initial image and the unknown initial Hamiltonian momentum respectively, K is a chosen smoothing kernel, $w_i > 0$ scalar weights and Y_i is the measured image at time t_i; $d^2(A, B)$ denotes a squared distance(-like) image similarity measure between the two images A and B and can be one of the standard image similarity measures or can be based on image registration itself to allow for large deviations between the geodesic regression line and the Y_i [7]. A numerical scheme using registration-based distances can be derived, but is impractical, because it would require frequent

[1] This is a simplifying assumption akin to formulating a growth model with respect to an initial image.

costly recomputations of the distances in an iterative solution scheme. Hence, an approximation of the registration-based distance is desirable. We define the squared distance [1] as

$$d^2\ (A,B) = \frac{1}{2}\int_0^1 \|v^*\|_L^2\ dt, \text{ where} \tag{6}$$
$$v^* = \underset{v}{argmin}\ \frac{1}{2}\int_0^1 \|v\|_L^2\ dt + \frac{1}{\sigma^2}\|I(1)-B\|_2^2, \text{ s.t. } I_t + \nabla I^T v = 0,\ I(0) = A.$$

This is an inexact matching formulation since an exact matching is typically impossible by a spatial transformation alone due to noise and appearance changes[2].

To simplify the geodesic regression formulation (4) we use a first order approximation of pairwise distances [9]. In contrast to [9], the time-series aspect of the images has to be considered. For all pairwise distances, $I(t_0)$ becomes the base image. For two images A, B and given spatial transformations $\Phi_t^{v_0^A}$ and $\Phi_t^{v_0^B}$ which map $I(t_0)$ to A and B in time t, the composition $\Phi_t = \Phi_t^{v_0^B} \circ (\Phi_t^{v_0^A})^{-1}$ maps A to B. Since both transformations are parameterized by initial velocity fields v_0^A and v_0^B respectively, we approximate Φ_t to first order as

$$\Phi_t = \mathrm{Exp}_{\mathrm{Id}}(tv_0^B) \circ \mathrm{Exp}_{\mathrm{Id}}(-tv_0^A) \approx \mathrm{Exp}_{\mathrm{Id}}(t(v_0^B - v_0^A)). \tag{7}$$

Then the squared distance can be approximated as

$$d^2(A,B) \approx \frac{1}{2}t^2\langle K^{-1}(v_0^B - v_0^A), v_0^B - v_0^A\rangle \tag{8}$$

or in momentum form

$$d^2(A,B) \approx \frac{1}{2}t^2\langle (p(t_0)^B - p(t_0)^A)\nabla I(t_0), K((p(t_0)^B - p(t_0)^A)\nabla I(t_0)\rangle. \tag{9}$$

Using this approximation to rewrite the geodesic regression formulation (4) yields

$$E(I(t_0), p(t_0)) = \frac{1}{2}\langle p(t_0)\nabla I(t_0), K(p(t_0)\nabla I(t_0))\rangle$$
$$+ \sum w_i \frac{1}{2}(t_i - t_0)^2\langle (p(t_0)^{Y_i} - p(t_0))\nabla I(t_0), K((p(t_0)^{Y_i} - p(t_0))\nabla I(t_0)\rangle. \tag{10}$$

We assume that $I(t_0)$ is on the geodesic[3]. All $p(t_0)^{Y_i}$ are precomputed by pairwise registrations with $I(t_0)$. The approximated energy only depends on the initial momentum $p(t_0)$. Taking the variation of (10) with respect to $p(t_0)$ results in

$$\delta E(I(t_0), p(t_0); \delta p) = \langle \nabla I(t_0)^T K m(t_0), \delta p\rangle$$
$$+ \sum w_i (t_i - t_0)^2 \langle \nabla I(t_0)^T K(m_i(t_0) - m(t_0)), -\delta p\rangle, \tag{11}$$

[2] A metamorphosis approach [10] could be used instead.

[3] Otherwise registrations between $I(t_0)$ and all other images would be required when $I(t_0)$ changes, providing no benefit over the original geodesic regression method. This is a simplifying assumption, which transforms the model into a type of growth model described by a geodesic.

where K is assumed to be a symmetric kernel, $m(t_0) = p(t_0)\nabla I(t_0)$ and $m_i(t_0) = p(t_0)^{Y_i}\nabla I(t_0)$. Collecting terms yields

$$\delta E(I(t_0), p(t_0); \delta p) = \langle \nabla I(t_0)^T K[m(t_0) + \sum w_i(t_i - t_0)^2(m(t_0) - m_i(t_0))], \delta p \rangle. \tag{12}$$

For a candidate minimizer δE needs to vanish for any admissible δp. Hence,

$$m(t_0) + \sum w_i(t_i - t_0)^2(m(t_0) - m_i(t_0)) = 0 \tag{13}$$

or in momentum space

$$p(t_0) + \sum w_i(t_i - t_0)^2(p(t_0) - p(t_0)^{Y_i}) = 0. \tag{14}$$

Solving for $p(t_0)$ results in

$$p(t_0) = \frac{\sum w_i(t_i - t_0)^2 p(t_0)^{Y_i}}{1 + \sum w_i(t_i - t_0)^2}. \tag{15}$$

In practice most frequently, $w_i = w = const$ and $w >> 1$ simplifying (15) to

$$p(t_0) \approx \frac{\sum (t_i - t_0)^2 p(t_0)^{Y_i}}{\sum (t_i - t_0)^2}, \tag{16}$$

which is a simple averaging of the initial momenta with weights $g_i = \frac{(t_i - t_0)^2}{\sum (t_i - t_0)^2}$. This formulation recovers the original image-to-image registration result for the special case of two images. To obtain the initial momenta $p(t_0)^{Y_i}$ which are needed to approximate the registration distance at time t_i one could modify the registration problem (6) by integrating between t_0 and t_i and solve it with the algorithm proposed in [1]. However, such an approach would suffer from two short-comings: (i) it would not guarantee geodesic solutions and (ii) the relative weighting of the image similarity measure would be influenced by the different time-periods used to perform the deformations (since $\|v\|_L^2$ is integrated over time, the same deformation becomes cheaper for a longer time interval). We therefore use (i) a shooting method [11] to compute the registrations and (ii) compute $\overline{p}(t_0)^{Y_i}$ by registering $I(t_0)$ to Y_i in unit time followed by a rescaling of the momentum to account for the original time duration: $p(t_0)^{Y_i} = \frac{1}{t_i - t_0}\overline{p}(t_0)^{Y_i}$. Using the momenta computed for a unit time, the initial momentum for the regression geodesic can be written as

$$p(t_0) \approx \frac{\sum (t_i - t_0)\overline{p}(t_0)^{Y_i}}{\sum (t_i - t_0)^2}. \tag{17}$$

Given the base image $I(t_0)$ and $p(t_0)$, we can integrate Eq. (5) forward or backward in time to obtain the regression geodesic. Our approximate geodesic regression results in a dramatic simplification of the optimization method for geodesic regression. Pairwise registrations can be computed in parallel if desired.

4 Experiments

Implementation. In the following experiments, the smoothing kernel K is set as the weighted sum of N Gaussian kernels K_{σ_n} [12]: $K(x) = \sum_{n=1}^{N} c_n K_{\sigma_n}(x)$, $c_n = c'_n / g(K_{\sigma_n}, I_S, I_T)$. Usually we set $c'_n = 1$. We first compute c_n for image pairs (following [12]) and then take the average of all the c_n as the weights for the kernels. All images are slightly blurred before registration.

Synthetic Images. In the first experiment, we synthesized the movement of a bull's eye using a series of 2D binary images (32×32 pixels, spacing 0.04) as shown in Fig. (2). The white circle inside of the eye grows at a constant speed while the outside white loop shrinks. We used four images at time instants 0, 10, 20, 30s, $I(0)$ as the base image, and 7 Gaussian kernels for K, $\{K_{0.5}, K_{0.4}, K_{0.3}, K_{0.2}, K_{0.15}, K_{0.1}, K_{0.05}\}$; $\sigma^2 = 0.01$. The simple geodesic regression result (2nd row of Fig. (2)) shows that changes are captured well.

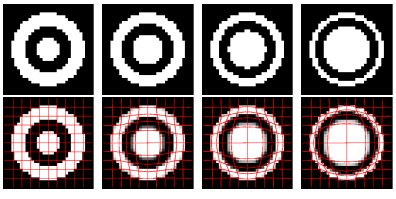

Fig. 2. Synthetic bull's eye experiment (top row) and results for simple geodesic regression (bottom row). The movement is well captured.

To quantify the regression accuracy we compute the overlay error between measurement images and the images on the geodesic:

$$E_{overlay}(I(t_i), Y_i) = \frac{1}{|\Omega|} ||\epsilon(I(t_i), Y_i)||_{L^1}, \quad \epsilon(I, J)(x) = |I(x) - J(x)|. \tag{18}$$

Table 1. Comparison of overlay errors among image pairs, the original geodesic regression, and our simple geodesic regression

	$E_{overlay}(I(t_i), Y_i)$			
Measurement Images	Y_0	Y_1	Y_2	Y_3
Image pairs($I(t_i) = Y_0, Y_i$)	0	0.0820	0.1914	0.3242
OGR(fixed initial image: Y_0)	0	0.0247	0.0306	0.0311
SGR(base image: Y_0)	0	0.0274	0.0329	0.0261

Tab. 1 shows the overlay errors between the initial image and all other measurements, the results of the original geodesic regression (OGR) and of the simple geodesic regression (SGR) regression respectively. The regression models are comparable in accuracy indicating that SGR works correctly in this experiment.

To illustrate the necessity of using a registration-based distance rather than the squared L^2 distance of two images, two test cases in Fig. 3 are employed for comparing the results of the original geodesic regression and our method. In the cases, five binary images (64×64 pixels, spacing 0.02) are generated to describe a square moving from left to right at uniform speed without oscillation (subfigure (a)) and with strong vertical oscillation by a constant amplitude (subfigure (b)). Here, K is $\{K_1, K_{0.75}, K_{0.5}, K_{0.4}, K_{0.3}, K_{0.2}, K_{0.15}, K_{0.1}\}$.

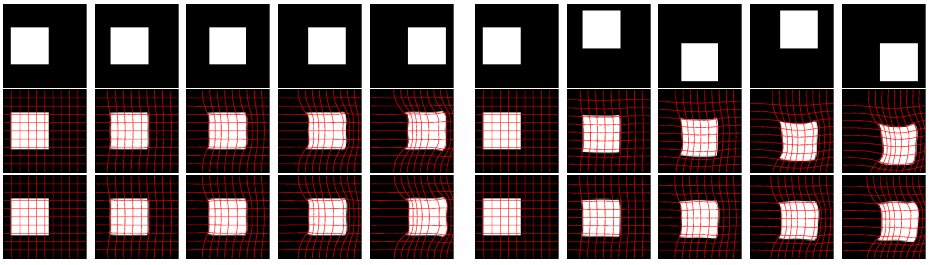

(a) (b)

Fig. 3. Square moving from left to right without oscillation (a) and with vertical oscillation (b). Top: original images. Middle: the results of the original geodesic regression. Bottom: the results of our method.

When there is no oscillation in the movement (Fig. 3(a)), the original geodesic regression has comparable performance to our method. In case (b), similar to the regression lines for the scalar case (Fig. 4), the square is expected to move to the right while moving down slightly, which is consistent with the SGR result (bottom row of subfigure (b)). However, the square in the original geodesic regression (using the L^2 distance) leads to a stronger shape deformation and deviation from the horizontal line.

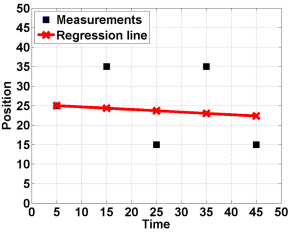

Fig. 4. Scalar experiment

Fig. 5 compares the proposed weighting of initial momenta for SGR (Eq. (16)) to a direct arithmetic average for a set of 3 images (64×64 pixels; spacing 0.02) at time points 0, 10, 40s respectively. The images at 10s and 40s are displaced by an equal distance vertically with respect to the image at 0s, but the horizontal displacements differ by a factor of 3. We chose the same multi-Gaussian kernel as in the first experiment. The SGR weighting is clearly more appropriate.

Real Images. We also evaluated SGR on two sets of longitudinal magnetic resonance images: 2D slices of a longitudinal dataset from the OASIS database and a 3D longitudinal dataset from a macaque monkey. One K, $\{K_{3.0}, K_{1.5}, K_{0.5}, K_{0.4}, K_{0.3}, K_{0.2}, K_{0.1}, K_{0.05}\}$, was applied to all the real images[4].
The four images in the first row of Fig. 6(a) are slices from an OASIS data set (161×128 pixels, spacing 0.5) for a subject scanned at age 67, 68, 71, and 73. We applied SGR with the youngest slice as the base image. The changes between the base image and other measurements are subtle, as illustrated by the difference images in the left column of Fig. 6(b) and the overlay errors in the first row of Tab. 2. However, our method successfully captures the variations in the brain images, especially the ventricle expansion, which is supported by the generated images (Fig. 6(a), 2nd row) and the difference images (right column Fig. 6(b)).

[4] Slightly better results may be achievable by data-set-dependent tuning of the kernel.

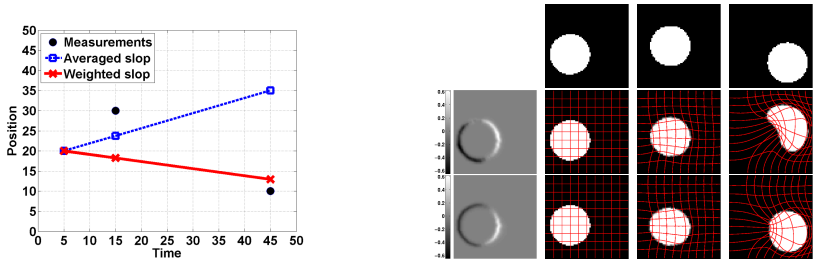

(a) (b)

Fig. 5. Scalar and image-valued cases comparing arithmetic averaging and the proposed weighting approach for initial momenta. (a) Scalar case. (b) Image case: image time-series (0, 10, 40s) (top), the initial momentum and the images generated by simply averaging the initial momenta (middle) and by our weighting method (bottom).

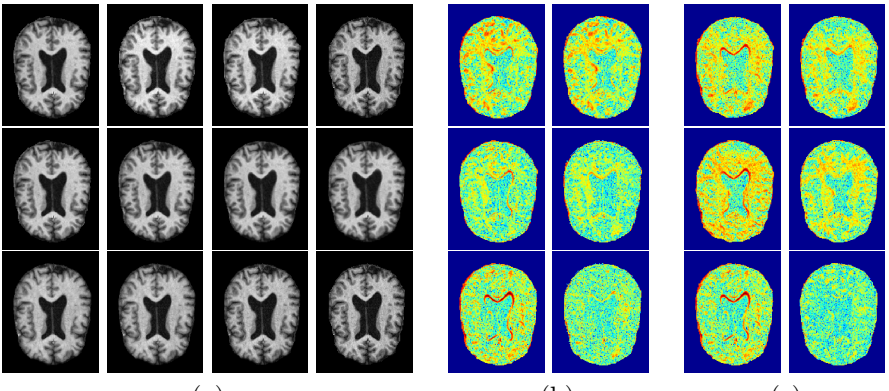

(a) (b) (c)

Fig. 6. OASIS data: (a): Original images (top, left to right: 67, 68, 71, 73 [years]), geodesic I with youngest slice as base image (middle), and geodesic II with oldest slice as base image (bottom). (b): Difference images of measurement images (up to down: 68, 71, 73 [years]) with youngest image (left) and images on geodesic I (right). (c): Difference images of measurement images (up to down: 71, 68, 67 [years]) with oldest image (left) and images on the geodesic II (right).

We also took the oldest slice as the base image to verify the efficiency of our model. As shown by the generated trajectory (Fig. 6(a), 3rd row), the difference images (Fig. 6(c)), and overlay errors in Tab. 2, our method works well.

The images ($150 \times 125 \times 100$ pixels with spacing 0.5468) in Fig. 7 are from a longitudinal data-set of a macaque monkey at the age of 3, 6, 12 and 18 months respectively[5]. We set the image at 3 months as the base image and applied our approach to capture the changes of the ventricle marked by the magenta

[5] Note that this is a time-range of active brain myelination for the macaque. Hence image intensities for the white matter are not constant over time and therefore a perfect image match is not expected.

Table 2. Overlay error among image pairs, the original geodesic regression (OGR), and our simple geodesic regression (SGR) for longitudinal subject data shown in Fig. 6

	$E_{overlay}(I(t_i), Y_i)$			
Measurement Images [Years]	$Y_0 = 67$	$Y_1 = 68$	$Y_2 = 71$	$Y_3 = 73$
Image pairs ($I(t_i) = Y_0, Y_i$)	0	0.0468	0.0342	0.0472
OGR (fixed initial image: Y_0)	0	0.0452	0.0298	0.0313
SGR (base image: Y_0)	0	0.0449	0.0304	0.0286
Measurement Images [Years]	$Y_0 = 73$	$Y_1 = 71$	$Y_2 = 68$	$Y_3 = 67$
Image pairs ($I(t_i) = Y_0, Y_i$)	0	0.0536	0.0631	0.0472
OGR (fixed initial image: Y_0)	0	0.0448	0.0457	0.0284
SGR (base image: Y_0)	0	0.0438	0.0432	0.0258

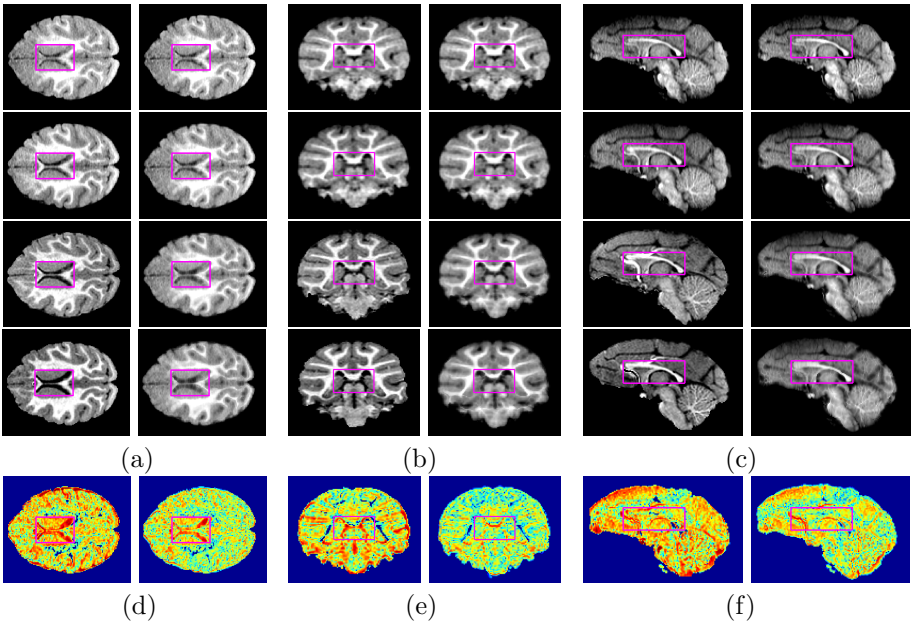

Fig. 7. Results for the macaque monkey data (up to down: 3, 6, 12, 18 [months], the youngest one as base image). (a-c): axial, coronal and sagittal slices of the original images (left) and images on the geodesic (right). (d-f): difference images of the oldest image with the youngest one (left) and with the images on the geodesic (right).

windows. As the monkey's age increases, the ventricle gradually approaches the edges of the windows, which is well captured by SGR.

5 Discussion and Conclusions

We developed a simplified geodesic regression model by approximating the squared distances between the regression geodesic and the measurement images.

In contrast to the original geodesic regression formulation for images, SGR can be efficiently computed. In fact, it only requires pair-wise registrations of the measurement images with respect to a chosen base-image (typically either the first or the last image of a time-series). The regression geodesic is then determined by the base image and the initial momentum obtained by appropriate averaging of the initial momenta of the pairwise registrations. Future work will focus on using this regression model for longitudinal image-based population-studies and on extending it to capture spatial and appearance changes simultaneously.

Acknowledgments. This work was sponsored by NSF EECS-1148870, NSF EECS-0925875, NIH NIHM 5R01MH091645-02, NIH NIBIB 5P41EB002025-28, NIH NHLBI 5R01HL105241-02 and U54 EB005149.

References

1. Beg, M.F., Miller, M.I., Trouvé, A., Younes, L.: Computing large deformation metric mappings via geodesic flows of diffeomorphisms. International Journal of Computer Vision 61(2), 139–157 (2005)
2. Durrleman, S., Pennec, X., Trouvé, A., Gerig, G., Ayache, N.: Spatiotemporal Atlas Estimation for Developmental Delay Detection in Longitudinal Datasets. In: Yang, G.-Z., Hawkes, D., Rueckert, D., Noble, A., Taylor, C. (eds.) MICCAI 2009, Part I. LNCS, vol. 5761, pp. 297–304. Springer, Heidelberg (2009)
3. Niethammer, M., Hart, G., Zach, C.: An optimal control approach for the registration of image time series. In: Conference on Decision and Control (CDC), pp. 2427–2434. IEEE (2009)
4. Trouvé, A., Vialard, F.X.: Shape splines and stochastic shape evolutions: A second order point of view. Arxiv preprint arXiv:1003.3895 (2010)
5. Fishbaugh, J., Durrleman, S., Gerig, G.: Estimation of Smooth Growth Trajectories with Controlled Acceleration from Time Series Shape Data. In: Fichtinger, G., Martel, A., Peters, T. (eds.) MICCAI 2011, Part II. LNCS, vol. 6892, pp. 401–408. Springer, Heidelberg (2011)
6. Davis, B.C., Fletcher, P.T., Bullitt, E., Joshi, S.: Population Shape Regression from Random Design Data. In: 11th IEEE ICCV (2007)
7. Niethammer, M., Huang, Y., Vialard, F.-X.: Geodesic Regression for Image Time-Series. In: Fichtinger, G., Martel, A., Peters, T. (eds.) MICCAI 2011, Part II. LNCS, vol. 6892, pp. 655–662. Springer, Heidelberg (2011)
8. Fletcher, P.T.: Geodesic regression on Riemannian manifolds. In: Proceedings of International Workshop on Mathematical Foundations of Computational Anatomy, MFCA (2011)
9. Yang, X., Goh, A., Qiu, A.: Approximations of the Diffeomorphic Metric and Their Applications in Shape Learning. In: Székely, G., Hahn, H.K. (eds.) IPMI 2011. LNCS, vol. 6801, pp. 257–270. Springer, Heidelberg (2011)
10. Trouvé, A., Younes, L.: Metamorphoses through Lie group action. Foundations of Computational Mathematics 5(2), 173–198 (2005)
11. Vialard, F.X., Risser, L., Rueckert, D., Cotter, C.J.: Diffeomorphic 3D image registration via geodesic shooting using an efficient adjoint calculation. International Journal of Computer Vision, 1–13 (2011)
12. Risser, L., Vialard, F.-X., Wolz, R., Murgasova, M., Holm, D.D., Rueckert, D.: Simultaneous Multi-Scale Registration Using Large Deformation Diffeomorphic Metric Mapping. IEEE Transcations on Medical Imaging 30(10), 1746–1759 (2011)